Adsorption of Tetraphenylphosphonium and Tetraphenylborate in Self-Assembled Phosphatidylcholine and Phosphatidylserine Monolayers Deposited on Mercury Electrodes

ARTICLE *in* THE JOURNAL OF PHYSICAL CHEMISTRY · JUNE 1995

Impact Factor: 2.78 · DOI: 10.1021/j100024a042

4 AUTHORS, INCLUDING:

Maria Rosa Moncelli
University of Florence
121 PUBLICATIONS **2,036** CITATIONS
SEE PROFILE

Lucia Becucci
University of Florence
72 PUBLICATIONS **1,368** CITATIONS
SEE PROFILE

Rolando Guidelli
University of Florence
226 PUBLICATIONS **3,816** CITATIONS
SEE PROFILE

Adsorption of Tetraphenylphosphonium and Tetraphenylborate in Self-Assembled Phosphatidylcholine and Phosphatidylserine Monolayers Deposited on Mercury Electrodes

Maria Rosa Moncelli, Roberto Herrero, Lucia Becucci, and Rolando Guidelli

J. Phys. Chem., **1995**, 99 (24), 9940-9951 • DOI: 10.1021/j100024a042

Adsorption of Tetraphenylphosphonium and Tetraphenylborate in Self-Assembled Phosphatidylcholine and Phosphatidylserine Monolayers Deposited on Mercury Electrodes

Maria Rosa Moncelli, Roberto Herrero,† Lucia Becucci, and Rolando Guidelli*

Department of Chemistry, Florence University, Florence, Italy

Received: December 14, 1994; In Final Form: March 7, 1995[⊗]

The adsorption of tetraphenylborate ($TPhB^-$) and tetraphenylphosphonium ($TPhP^+$) ions in self-assembled monolayers of phosphatidylcholine (PC) and phosphatidylserine (PS) deposited on a mercury electrode was estimated by measuring the time dependence of the charge which flows as a consequence of potential steps causing ion translocation across the monolayer. In the time scale of 100 ms, the translocation of $TPhP^+$ ions is controlled by diffusion from the bathing solution, while that of $TPhB^-$ ions is primarily controlled by the adsorption into the polar head region. Deviations from the Henry isotherm behavior were interpreted on the basis of an adsorption isotherm which accounts both for discreteness-of-charge effects and for the presence of two regions of different dielectric constant ϵ, i.e., the hydrocarbon tail region ($\epsilon \approx 2$) and the polar head region ($\epsilon_2 = 8-30$). This isotherm also interprets a number of data for ionic adsorption in bilayers available in the literature using reasonable values for the parameters of lipid layers. The pH dependence of the adsorption coefficient of $TPhP^+$ and $TPhB^-$ ions in PS monolayers points to changes in the conformation and in the acidic properties of the polar heads of this lipid induced by ionic adsorption.

Introduction

The transport of lipophilic ions across bilayer lipid membranes (BLMs) has been extensively studied both from a kinetic point of view and with the aim of determining the amount of ions adsorbed within the two polar head regions of BLMs.[1-9] In general, this transport is assumed to require the passage over a central energy barrier separating two deep energy wells located within the two polar head regions. If the membrane is symmetric, the energy barrier is also assumed to be symmetric. The kinetics of transport in relaxation experiments is often tackled by solving the generalized time-dependent Nernst−Planck equation under the simplifing assumption that the lipophilic ions are almost completely located within the energy wells; the additional assumptions that the transmembrane potential is small with respect to RT/F[1,5,8] and that the electric field varies linearly between the two energy wells are also frequently made.[2,3] The potential difference between the two energy wells is usually considered to be a constant fraction of the transmembrane potential, although Andersen et al.[6] used a three-capacitor model to show that this fraction depends on the amounts of ions in the two energy wells and hence varies during their translocation.

The kinetics of translocation of ions through the membrane in relaxation experiments is generally assumed to involve three steps: namely, (i) adsorption of the ions in the polar head region on one side of the membrane, (ii) surmounting of the intermediate energy barrier with the resulting translocation to the polar head region on the other side of the membrane, and (iii) desorption from the latter polar head region into the adjacent bathing solution. In the case of dipicrylamine (DpA^-) and tetraphenylborate ($TPhB^-$), translocation across a dioleoylphosphatidylcholine bilayer, potential step experiments have shown that the rate-determining step is step iii, namely, ion desorption into the bathing solution.[1] However, by using potential steps of short duration and very low concentrations of the liphophilic ions in the bathing solutions, the kinetic study can be focused exclusively on the translocation step ii, since step iii becomes too slow to be operative.[3] Under these experimental conditions, only a capacitive current flows across the membrane and the number of ions adsorbed in it remains constant, but at the end of the potential step the current has not yet attained its minimum stationary value.

So far ion transport systems have been usually studied using symmetric BLMs. A more recent model of biomembranes is represented by a phospholipid coated mercury electrode.[10,11] The phospholipid coating is provided by spreading a solution of the phospholipid in a suitable solvent (e.g., pentane) on the surface of an aqueous electrolyte, allowing the solvent to evaporate, and immersing a hanging mercury drop electrode in the electrolyte. This procedure gives rise to half a self-assembled bilayer, with the hydrocarbon tails directed toward the metal and the polar heads directed toward the solution. Self-assembled phospholipid monolayers on mercury electrodes offer some advantages over BLMs, when used as biomimetic membranes. Thus, the electric potential and the ion flux across these monolayers can be controlled more accurately and more directly than across BLMs. Moreover, these half-membranes provide an inherent mechanical stability and a resistance to high electric fields which is not shared by BLMs. Over the region of minimum capacity, the film is impermeable to inorganic metal ions, whereas it becomes permeable outside this region. By measuring the differential capacity C of these lipid monolayers supported on mercury, we have recently determined the intrinsic protonation constants of the ionizable groups of phosphatidylcholine (PC), phosphatidylethanolamine (PE), and phosphatidylserine (PS).[12] It was thus shown that PS monolayers bear only a small negative charge at the physiological pH, are practically neutral around pH 6, and become slightly positively charged at lower pH values. These results, obtained with PS monolayers with a rigorously constant cross-sectional area per lipid molecule and in the absence of any incorporated lipophilic molecules, contrast with literature data according to which PS mono- or bilayers are negatively charged at pH > 2.[13-16] This led us to conclude that even slight perturbations may induce conformational changes in the PS polar heads which are

† On leave from the Departamento de Química Fundamental e Industrial, Universidade da Coruña, A Coruña, Spain.

[⊗] Abstract published in *Advance ACS Abstracts,* May 1, 1995.

0022-3654/95/2099-9940$09.00/0

accompanied by appreciable changes in the acidic properties of the corresponding ionizable groups.

The present note reports an investigation of the adsorption of the $TPhB^-$ anion and of the tetraphenylphosphonium cation ($TPhP^+$) within the polar head region of self-assembled monolayers of PC and PS. To this end, the differential capacity C of the monolayers was measured as a function of the applied potential E; moreover, the charge $Q(t)$ flowing along the external circuit as a consequence of a series of potential steps ΔE of different width was measured as a function of time t using a wholly computerized chronocoulometric apparatus.

Experimental Section

The adsorbed monolayers of PC and PS on mercury were prepared as described by Nelson and Auffret.[17,18] The water used was obtained from light mineral water by distilling it once, and then distilling the water so obtained from alkaline permanganate, while constantly discarding the heads. Merck reagent grade KCl was baked at 500 °C before use to remove any organic impurities. Dioleoyl PC and dioleoyl PS were obtained from Lipid Products (South Nutfield, Surrey, England). All measurements were carried out in aqueous solutions of 0.1 M KCl at 25 ± 0.1 °C. The solutions were buffered with PS and unbuffered with PC; in the latter case, the pH was constantly found to range from 4.8 to 5.3. The desired pH values were realized with Merck suprapur HCl over the pH range from 2 to 5, with a 1×10^{-3} M $HPO_4^{2-}/H_2PO_4^-$ buffer over the pH range from 6.5 to 7.5 and with a 1×10^{-3} M H_3BO_3/NaOH buffer over the pH range from 8.5 to 9.

The home-made hanging mercury drop electrode (HMDE) employed in our measurements, the cell, and the detailed procedure to produce self-organized lipid monolayers deposited on mercury are described elsewhere.[12] Differential capacity measurements were carried out using a Metrohm Polarecord E506 (Herisau, Switzerland). The ac signal had a 10 mV amplitude and a 75 Hz frequency. The system was calibrated using a precision capacitor. All potentials were measured versus a saturated calomel electrode (SCE).

The computerized chronocoulometric apparatus is described elsewhere.[19] The microprocessor used to control all the operations was a Model NOVA 4X from Data General (Westboro, MA), whereas an Amel Model 551 (Milano, Italy) fast rise potentiostat with a rise time ≤ 0.1 μs was employed for the potentiostatic control of the three-electrode system. The detailed scheme of the home-made electronic current integrator working under microprocessor control is described in ref 20. The chronocoulometric measurements consisted of a series of consecutive potential steps of progressively increasing width from a fixed initial value E_i to different final values E; each series was carried out on a single lipid coated mercury drop. The initial potential E_i was chosen to be positive (negative) enough to prevent adsorption of $TPhP^+$ ($TPhB^-$) directly on the mercury surface, while allowing ionic adsorption in the polar head region under equilibrium conditions. After 100 ms from each $E_i \rightarrow E$ potential step, the potential was stepped back from E to E_i and kept at E_i for 10 s, in order to restore the initial equilibrium conditions; the current $i(E,t)$ flowing as a consequence of each forward potential step $E_i \rightarrow E$ was integrated electronically, and the resulting charge $Q(E,t)$ was stored in the microprocessor memory as a function of the time t elapsed from the instant of the corresponding $E_i \rightarrow E$ potential step. To ensure the attainment of adsorption equilibrium of the lipophilic ions in the polar head region at E_i, the bathing solution was first subjected to mild stirring for different time lengths τ, and the corresponding charge $Q(E,t)$ was then measured; at any given time t, this quantity was found to increase progressively with τ attaining a maximum limiting value for τ values greater than a certain minimum value τ_{min}. Owing to mass transport control of ionic adsorption, τ_{min} was found to decrease rapidly with an increase in the bulk ionic concentration, c. Each series of chronocoulometric measurements at constant c was carried out after stirring the solution at E_i for a time period greater than the corresponding τ_{min} value. At the lowest ionic concentration investigated, $c = 1 \times 10^{-7}$ M, τ_{min} was found to be about equal to 4 min.

Results

In the absence of lipophilic ions, the differential capacity C at the lipid coated electrode varies only very slightly over the potential region of minimum capacity, namely, from −0.2 to −0.8 V. Conversely, in the presence of these ions C shows a hump which develops on the negative side of this potential region in the case of $TPhP^+$ in PC and PS monolayers, and on the positive side in the case of $TPhB^-$ in PS monolayers. The presence of $TPhB^-$ in PC monolayers gives rise to a shoulder simply because the hump merges with the steep rise exhibited in the proximity of −0.2 V by the differential capacity versus potential curve in the absence of $TPhB^-$. The capacity humps obtained with the $TPhP^+$ and $TPhB^-$ ions in PS monolayers are shown in Figure 1A, whereas those obtained in PC monolayers are shown in Figure 1B. Along these humps the in-phase component of the ac current was constantly found to be entirely negligible with respect to the quadrature component, thus excluding the presence of any Faradaic contributions.

The hump in the presence of TPhP+ ions was obtained by scanning the applied potential E in the negative direction after keeping the mercury drop under mild stirring at a potential positive to the hump for a time period $\tau > \tau_{min}$. It is clearly due to the charge displacement resulting from $TPhP^+$ translocation from the polar heads to the mercury surface and backward across the hydrocarbon tail region, following the ac signal superimposed on the bias potential E. Naturally, the to and fro movement of $TPhP^+$ cations following the ac signal is only possible at bias potentials E at which these ions are present both in the polar head region and on the mercury surface; this condition is not satisfied at potentials positive to the hump, where $TPhP^+$ is only present in the polar head region. In the case of the $TPhB^-$ anions, the applied potential E was scanned in the positive direction after keeping the mercury drop under mild stirring at a potential negative to the hump for a time period $\tau > \tau_{min}$.

Chronocoulometric curves of $Q(E,t)$ versus t for the translocation of 1×10^{-5} M $TPhP^+$ across a PS monolayer at pH 8.9 are shown in Figure 2; they were obtained by stepping the applied potential from a fixed initial value $E_i = -0.200$ V to different, regularly spaced final values. At final potentials E positive enough to prevent $TPhP^+$ translocation, the charge density $Q(E,t)$ undergoes an abrupt rise and then remains constant, since the capacitive current required to charge the whole interphase flows in less than 1 ms just after the $E_i \rightarrow E$ potential step. At potentials E at which $TPhP^+$ translocation starts to take place, the initial abrupt rise in charge is followed by a gradual increase in time, which becomes more pronounced as E is made progressively more negative. Ultimately, at sufficiently negative potentials, the $Q(E,t)$ versus t curves shift regularly upward with a further negative shift in E, while maintaining a constant shape. The $Q(E,t)$ versus t curves for $TPhP^+$ translocation across a PC monolayer exhibit the same behavior as those across a PS monolayer. All these curves provide linear $Q(t)$ versus $t^{1/2}$ plots whose slopes S increase

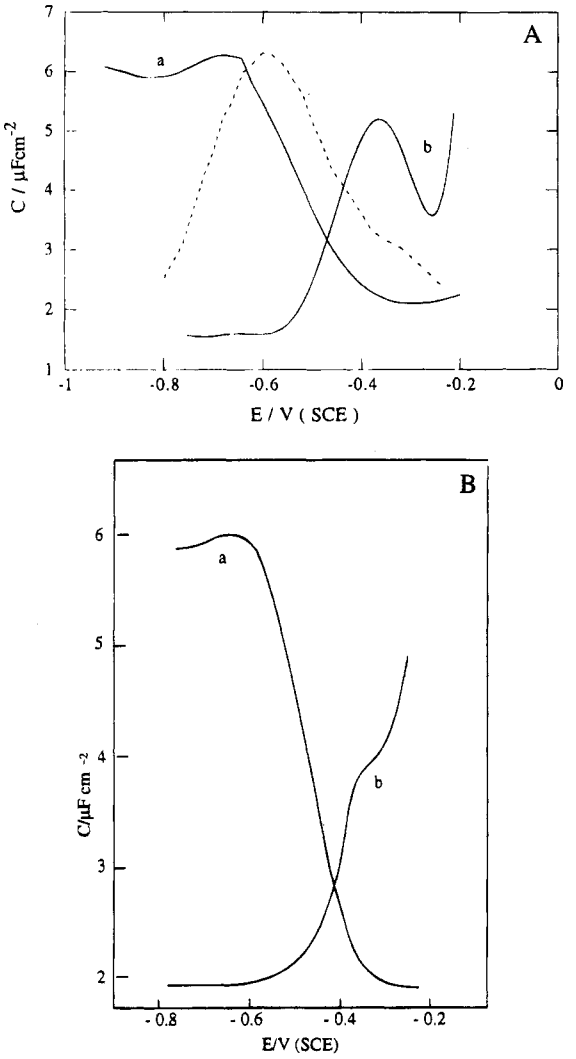

Figure 1. (A) C vs E curve for PS monolayers in contact with 1×10^{-5} M $TPhP^+$ at pH 8.9 (a) and with 6×10^{-6} M $TPhB^-$ at pH 2.7 (b). The dashed curve was calculated from the σ'_i vs E curve corresponding to the C vs E curve (a) using eq 10; $C_0 = 1.74$ μF cm^{-2} and $\sigma_i = 0.47$ μC cm^{-2}. (B) C vs E curve for PC monolayers in contact with 7×10^{-5} M $TPhP^+$ (a) and with 1×10^{-7} M $TPhB^-$ (b) in unbuffered solutions of 0.1 M KCl.

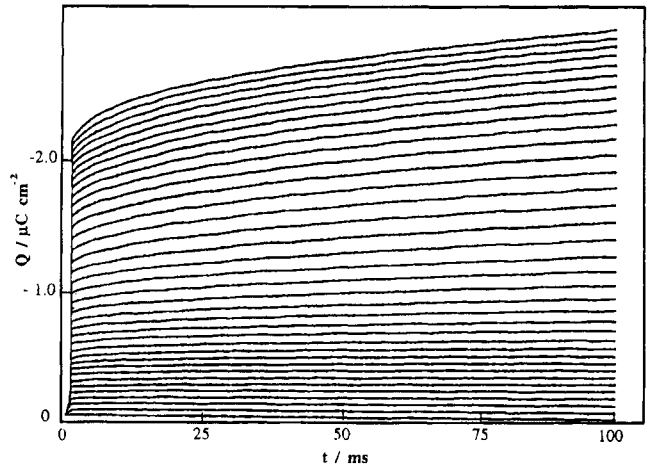

Figure 2. $Q(E,t)$ vs t curves for the translocation of 1×10^{-5} M $TPhP^+$ across a PS monolayer at pH 8.9, as obtained by stepping the potential from the fixed initial value $E_i = -0.200$ V to final values of E varying from -0.200 to -0.900 V by -20 mV increments.

proportionally to the bulk $TPhP^+$ concentration c, at least up to c values of the order of 1×10^{-4} M. At higher $TPhP^+$

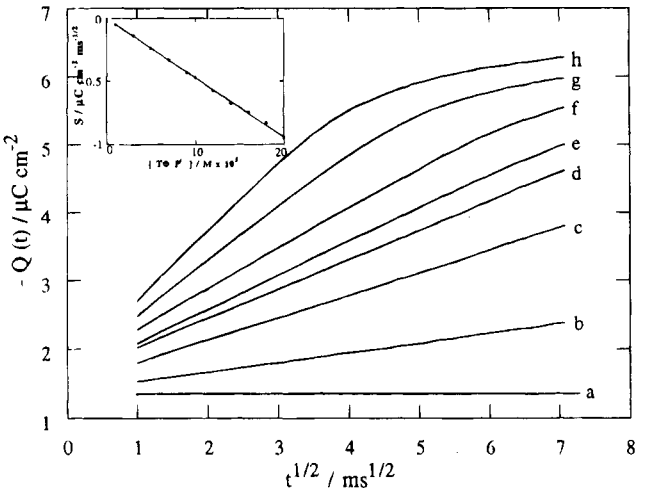

Figure 3. $Q(t)$ vs $t^{1/2}$ plots for the translocation of 0 (a), 3×10^{-5} (b), 7×10^{-5} (c), 9×10^{-5} (d), 1×10^{-4} (e), 1.2×10^{-4} (f), 1.6×10^{-4} (g), and 2×10^{-4} M (h) $TPhP^+$ across a PC monolayer following a potential step from $E_i = -0.200$ V to $E = -0.900$ V. The inset shows a plot of $S \equiv Q(t)/t^{1/2}$ vs c, whose constant slope equals -160 C cm $s^{-1/2}$ mol^{-1}.

concentrations, the $Q(t)$ versus $t^{1/2}$ plots start to deviate from linear behavior at progressively shorter times t with an increase in c (see Figure 3).

According to the Cottrell equation, a charge density $Q(t)$ which is diffusion controlled under limiting conditions is given by:

$$Q(t) = 2nF(Dt/\pi)^{1/2}c$$

where n is the number of faradays flowing along the external circuit in concomitance with the translocation of 1 mol of the lipophilic ion and D is the diffusion coefficient of the latter. If we apply this equation to the constant slope of the plot of $S = Q(t)/t^{1/2}$ versus c (see the inset of Figure 3), we obtain a reasonable value of $\approx 2 \times 10^{-6}$ cm^2/s for the diffusion coefficient D provided we set $n = -1$. The justification for the charge $Q(t)$ flowing along the external circuit being almost equal in magnitude and opposite in sign to that translocating across the lipid monolayer will be deffered to the Discussion. The present result points to a high rate of both the adsorption step of $TPhP^+$ ions into the polar head region and the subsequent translocation step, such that diffusion control is achieved in less than 1 ms from the instant of the potential step. The deviation of the $Q(t)$ versus $t^{1/2}$ plots from linear behavior at c values greater than about 1×10^{-4} M is simply due to the saturation of the adsorption sites on the mercury surface, which prevents a complete depletion of the polar head region after the negative potential step.

Extrapolation of the linear $Q(t)$ versus $t^{1/2}$ plots in Figure 3 to $t^{1/2} = 0$ yields an intercept which measures the charge along the external circuit due to the charging of the interphase following the potential step $E_i \rightarrow E$ and to the complete translocation of the $TPhP^+$ ions originally present in the polar head region. The intercepts for different bulk $TPhP^+$ concentrations c, as obtained by adopting a fixed potential step $E_i \rightarrow E$ negative enough to ensure complete translocation of the $TPhP^+$ ions initially adsorbed at $E_i = -0.200$ V, were measured relative to the intercept provided by the supporting electrolyte alone and then plotted against c, thus yielding the charge involved in this translocation; this is practically a measure of the charge σ_i of the $TPhP^+$ ions adsorbed at E_i as a function of c, namely, the adsorption isotherm of these ions in the polar head region

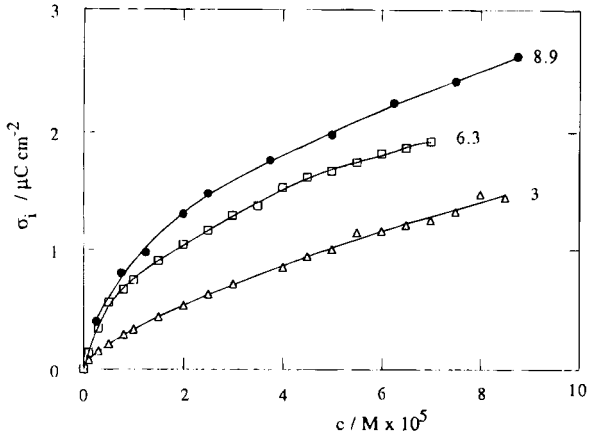

Figure 4. σ_i vs c plots for $TPhP^+$ adsorption in a PS monolayer. Numbers on each curve denote pH values.

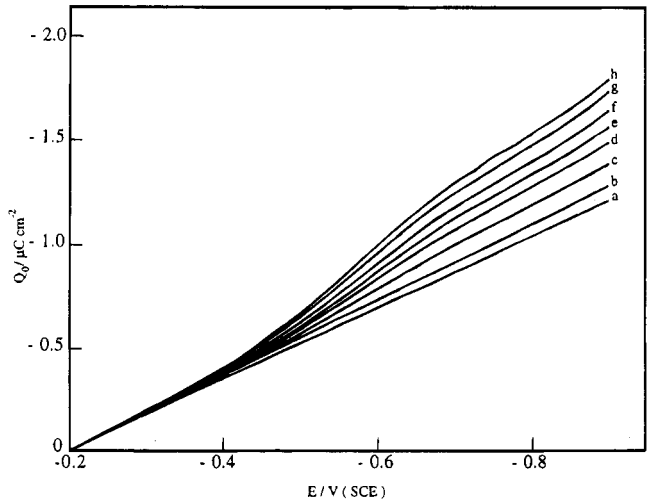

Figure 5. Q_0 vs E plots for the translocation of 0 (a), 1×10^{-7} (b), 1.75×10^{-6} (c), 3.4×10^{-6} (d), 5.05×10^{-6} (e), 6.7×10^{-6} (f), 8.35×10^{-6} (g), and 1×10^{-5} M (h) $TPhP^+$ across a PS monolayer at pH 4.

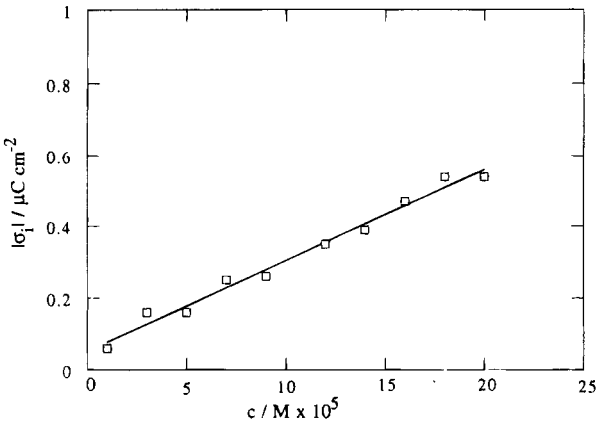

Figure 6. σ_i vs c plot for $TPhP^+$ adsorption in a PC monolayer from an unbuffered solution of 0.1 M KCl.

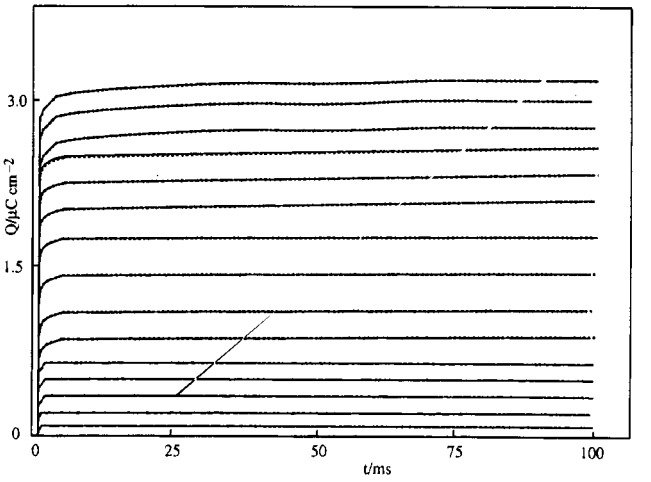

Figure 7. $Q(E,t)$ vs t curves for the translocation of 5×10^{-6} M $TPhB^-$ across a PC monolayer in an unbuffered solution of 0.1 M KCl, as obtained by stepping the potential from a fixed initial value $E_i = -0.750$ V to final values E varying from -0.750 to -0.150 V by 40 mV increments.

of the lipid monolayer. Figure 4 shows this plot for $TPhP^+$ adsorption in a PS monolayer at three different pH values.

Alternatively, the σ_i values were obtained by fitting to a straight line the $Q(t)$ versus $t^{1/2}$ plots relative to a series of potential steps from $E_i = -0.200$ V to different final potentials E (see, e.g., the series in Figure 2) and by plotting the corresponding intercepts Q_0 on the $t^{1/2} = 0$ axis against E. The resulting curves are shown in Figure 5; they exhibit a sigmoidal shape and their height, as measured from the curve of the supporting electrolyte alone, is once again a measure of σ_i. The accuracy of the extrapolation procedure along the rising portion of these curves, where the translocation of the $TPhP^+$ ions initially adsorbed at E_i is only partial, is not as good as that attained at the foot of these curves, where translocation still does not take place, or along their plateau, where such a translocation is complete. Since, however, the measured height of the Q_0 versus E curves in Figure 5 depends only on the foot and the plateau of these curves and not on their rising portion, the σ_i values obtained by the two alternative procedures are practically identical. The adsorptivity of $TPhP^+$ in PC is much less than in PS, as appears by comparing the σ_i versus c plot in Figure 6 for $TPhP^+$ adsorption in PC with the analogous plots in Figure 4.

The curves of $Q(E,t)$ versus t for the translocation of $TPhB^-$ across PS or PC monolayers, as obtained by stepping the potential from a fixed initial value $E_i = -0.750$ V to progressively more positive values E, exhibit a different behavior. This behavior is exemplified in Figure 7 for the case of $TPhB^-$ translocation across PC. At potentials at which $TPhB^-$ translocation takes place, the initial abrupt rise in charge is followed by a very slight, almost linear increase of $Q(t)$ with time, which depends only slightly upon the bulk $TPhB^-$ concentration, c. This indicates that the adsorption of the $TPhB^-$ anions in the polar head region is at least partially controlled by the adsorption step proper in the time scale of our chronocoulometric measurements. The adsorption isotherms of $TPhB^-$ in both PS and PC monolayers were therefore obtained by extrapolating to $t = 0$ the linear $Q(E,t)$ versus t plots relative to progressively more positive potential steps -0.750 V $\rightarrow E$ and by plotting the corresponding intercepts against E. The resulting plots have a sigmoidal shape just as those in Figure 5, and their height as measured from the plot of the supporting electrolyte alone provides a measure of σ_i. Plots of $|\sigma_i|$ versus c for $TPhB^-$ adsorption in PC and PS monolayers are shown in Figure 8, curves a and b.

All the above adsorption isotherms show a distinct initial linear portion (the Henry isotherm region) whose slope measures the adsorption coefficient K; K values relative to $TPhP^+$ and $TPhB^-$ adsorption in PC and PS monolayers at different pH values are summarized in Table 1. The K value for $TPhB^-$ in a PC monolayer, 6.5×10^{-3} cm, is intermediate between the two different values for $TPhB^-$ in a PE bilayer, $\approx 4 \times 10^{-3}$ cm and 3.7×10^{-2} cm, as estimated by Andersen and Fuchs[3] and Andersen et al.,[6] and is somewhat smaller than the K value for

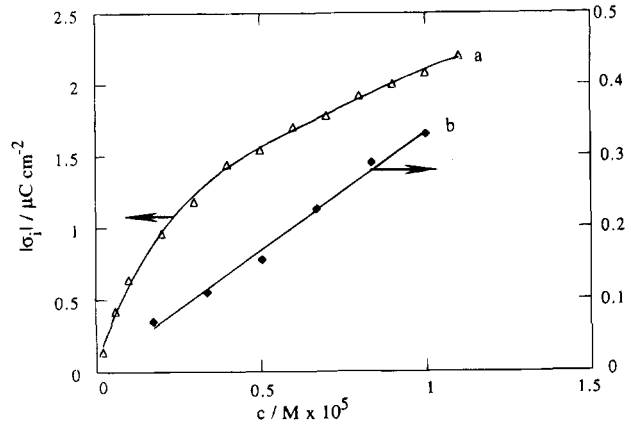

Figure 8. $|\sigma_i|$ vs c plots for the adsorption of $TPhB^-$ in a PC monolayer from an unbuffered solution of 0.1 M KCl (a), and in a PS monolayer from a pH 5 buffered solution of 0.1 M KCl (b). The arrows indicate the scales relative to each plot.

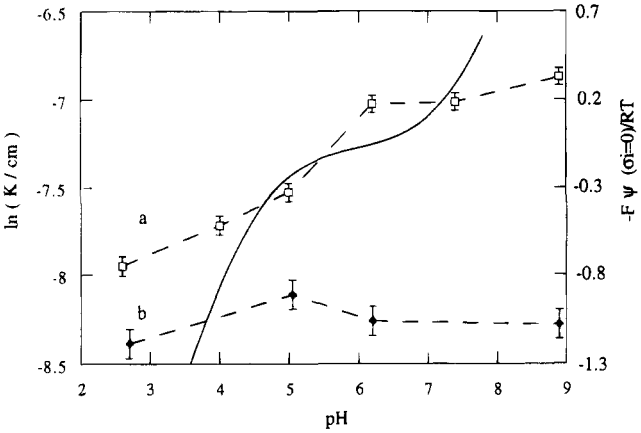

Figure 9. ln K vs pH plots for the adsorption of $TPhP^+$ (a) and $TPhB^-$ (b) in a PS monolayer. The solid curve is a plot of $-F\psi(\sigma_i=0)/RT$ vs pH calculated from eq 14 as described in the text.

TABLE 1: Adsorption Coefficients for $TPhP^+$ and $TPhB^-$ in PC and PS Monolayers (in cm)

	pH	K_{TPhP^+}	K_{TPhB^-}
PS	2.6	3.5×10^{-4}	2.3×10^{-4}
	4.0	4.5×10^{-4}	
	5.0	5.4×10^{-4}	3.0×10^{-4}
	6.2	8.9×10^{-4}	2.6×10^{-4}
	7.4	9.0×10^{-4}	
	8.9	1.0×10^{-3}	2.5×10^{-4}
PC	unbuffered solution	2.5×10^{-5}	6.5×10^{-3}

$TPhB^-$ in a PC bilayer, 2×10^{-2} cm, as estimated by Benz et al.[5] Note that the adsorption coefficient of $TPhB^-$ in PC is normally more that one order of magnitude greater than the other adsorption coefficients determined in this work. Figure 9 shows a plot of ln K versus pH for $TPhP^+$ adsorption in PS; note the relatively steep rise in ln K over the narrow pH range from 5 to 6, namely, over the pH range where PS monolayers were found to be electrically neutral on the basis of differential capacity measurements.[12]

Discussion

During the recording of differential capacity versus potential curves, translocation of the lipophilic ions takes place progressively in time along the hump; since the time required for such a recording is of a few tens of seconds, during this time ion translocation from the polar heads to the mercury surface will draw other ions (especially in the case of the $TPhP^+$ ions) into the polar head region by diffusion from the bulk, and then on the mercury surface. No such an inconvenience is encountered with chronocoulometric measurements, since the original equilibrium situation at the initial potential E_i is restored before each potential step $E_i \rightarrow E$, and any contribution to $Q(E,t)$ from ionic diffusion toward the lipid monolayer following the potential step is adequately corrected for.

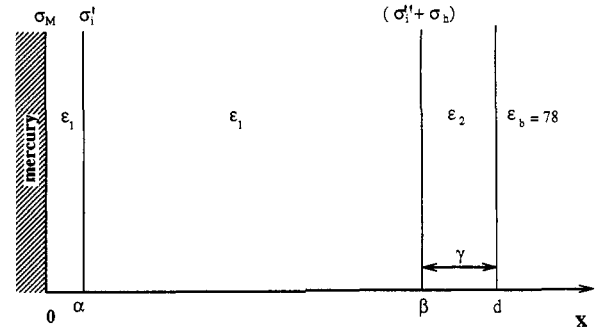

Figure 10. Schematic picture of a lipid monolayer deposited on mercury.

$TPhP^+$ adsorbs more rapidly than $TPhB^-$ from the bathing solution into the adjacent polar head region of PC and PS monolayers. This behavior is opposite to that observed with lipid bilayers, across which $TPhB^-$ is reported[21,22] to translocate several orders of magnitude more rapidly than $TPhP^+$. A tentative explanation for this difference in behavior, based on the different structure of lipid monolayers and bilayers, is the following. The polar heads of PC are characterized by the P−N dipoles roughly parallel to the lipid layer.[23] The penetration of bulky lipophilic ions across the polar head region is likely to involve a temporary reorientation of the above dipoles, with the negative end more or less turned toward the interior of the lipid layer in view of the closer vicinity of the phosphate group to the hydrocarbon tail region. The resulting negative potential difference will accelerate the adsorption of lipophilic cations while slowing down that of structurally similar anions. The final step in ion translocation across lipid bilayers consists of the desorption from the polar head region on the opposite side of the bilayer into the adjacent bathing solution. The temporary reorientation of the relative P−N dipoles with the positive end outward, which may accompany such a desorption, will now accelerate the desorption of anions and slow down that of cations. According to Läuger and co-workers,[1,5] the desorption from the polar head region into the aqueous phase is the rate-determing step in the transport of lipophilic ions across lipid bilayer membranes; if this is the case, then the above considerations may explain why the translocation rate of $TPhB^-$ across lipid bilayers is faster than that of $TPhP^+$.[21,22] On the other hand, the absence of a desorption step with these features in the translocation across lipid monolayers may cause the adsorption step in the polar head region to become the rate-determining step, thus justifying our observation that $TPhP^+$ adsorbs faster than $TPhB^-$ in lipid monolayers.

A Model. To interpret the behavior of the charge Q as a function of E, we shall make use of the simple three-capacitor model schematically depicted in Figure 10, in some respect similar to that proposed by Andersen et al.[6] for a planar bilayer. Here $x = 0$ is the mercury surface plane, where the metal charge density σ_M is located; $x = \alpha$ and $x = \beta$ are the loci of the centers of charge of the ions adsorbed on the mercury surface and in the polar head region, respectively; and $x = d$ is the plane separating the lipid monolayer from the bathing solution. Beyond this surface we find the diffuse layer, whose thickness $1/\kappa$ is provided by the Gouy−Chapman theory. The charge densities of the lipophilic ions adsorbed on the $x = \alpha$ and $x = \beta$ planes will be denoted by σ'_i and σ''_i; they will be regarded

as smeared out uniformly over these planes for simplicity. We will also make the further simplifying assumptions that the charge density σ_h due to the ionized groups of the polar heads of the lipid is located at $x = \beta$ and that the two layers ($0 < x < \alpha$) and ($\alpha < x < \beta$) are characterized by the same dielectric constant ϵ_1.

Denoting by ϵ_2 the dielectric constant over the polar head region $\beta < x < d$ and by $\epsilon_b = 78$ that of the aqueous solution, the potential difference Ψ_0 across the whole interphase is given by:

$$\Psi_0 = \frac{4\pi\alpha}{\epsilon_1}\sigma_M + \frac{4\pi(\beta-\alpha)}{\epsilon_1}(\sigma_M + \sigma'_i) + 4\pi\left(\frac{\gamma}{\epsilon_2} + \frac{1}{\epsilon_b\kappa}\right)(\sigma_M + \sigma_i + \sigma_h) = \frac{\sigma_M}{C} + \frac{\sigma'_i}{C_1} + \frac{\sigma_i + \sigma_h}{C_b} \quad (1)$$

with

$$\frac{1}{C} \equiv 4\pi\left(\frac{\beta}{\epsilon_1} + \frac{\gamma}{\epsilon_2} + \frac{1}{\epsilon_b\kappa}\right); \quad \frac{1}{C_1} \equiv \frac{4\pi(\beta-\alpha)}{\epsilon_1}; \quad \frac{1}{C_b} \equiv 4\pi\left(\frac{\gamma}{\epsilon_2} + \frac{1}{\epsilon_b\kappa}\right); \quad \sigma_i \equiv \sigma'_i + \sigma''_i; \quad \gamma \equiv d - \beta \quad (2)$$

Here σ_i is the overall charge density of the lipophilic ions on the $x = \alpha$ and $x = \beta$ planes; it is equal to their charge density within the polar head region in equilibrium with the corresponding bulk concentration c at the initial potantial E_i. σ_i can be regarded as constant independent of the width of the potential step $E_i \rightarrow E$ once the contribution from ionic diffusion is properly corrected for in chronocoulometric measurements. Such a correction will be constantly assumed in the following. It should be noted that the expression, $\Psi_d = 4\pi(\sigma_M + \sigma_i + \sigma_h)\kappa^{-1}/\epsilon_b$, for the ionic surface potential used in eq 1 results from the linearization of the Poisson-Boltzmann equation and hence overestimates $|\Psi_d|$ appreciably for $|\sigma_M + \sigma_i + \sigma_h|$ values greater than a few μC cm^{-2}. However, under the present experimental conditions, this approximation is acceptable because the Debye length κ^{-1} equals 9.6 Å in 0.1 M KCl; if we give γ and ϵ_2 the reasonable values 5 Å and 10, the γ/ϵ_2 term in the expression for $1/C_b$ of eq 2 is already four times greater than the approximate term $1/(\epsilon_b\kappa)$ accounting for the diffuse-layer contribution and would be even greater if the exact Gouy–Chapman expression for Ψ_d were employed. It should also be noted that $1/C_b$ is much less than both $1/C_1$ and $1/C$, because $(\beta - \alpha)$ is of the order of 20 Å and ϵ_1 is $\approx$2; hence the contribution from the $(\sigma_i + \sigma_h)/C_b$ term in eq 1 to the potential difference Ψ_0 across the whole interphase is small.

At E_i the ionic charge σ'_i in direct contact with the mercury surface equals zero and eq 1 reads:

$$\sigma_M = C\Psi_0 - \frac{C}{C_b}(\sigma_i + \sigma_h) \quad (3)$$

Conversely, after a sufficiently wide potential step $E_i \rightarrow E$, σ'_i becomes almost immediately equal to σ_i and eq 1 takes the form:

$$\sigma_M = C\Psi_0 - \frac{C}{C_1}\sigma_i - \frac{C}{C_b}(\sigma_i + \sigma_h) \quad (4)$$

The potential difference Ψ_0 across the whole interphase differs from the applied potential E by a constant depending exclusively on the choice of the reference electrode. Equations 3 and 4 show that the plot of $Q_0(E) = \sigma_M(E) - \sigma_M(E_i)$ against $E = (\Psi_0 + \text{constant})$ over the potential range preceding translocation and that over the potential range following complete translocation are expected to consist of parallel segments of slope C, separated by a vertical distance ΔQ_0 equal to

$$\Delta Q_0 = -\frac{C}{C_1}\sigma_i \approx -\frac{\beta-\alpha}{\beta}\sigma_i \quad (5)$$

This equation holds strictly if the charge density σ_h of the polar heads does not change during ion translocation and, hence, maintains the same value in eqs 3 and 4; however, even if this condition is not fulfilled, eq 5 retains a satisfactory validity because of the small contribution of the $-C(\sigma_i + \sigma_h)/C_b$ term in eqs 3 and 4.

In view of the preceding considerations, Q_0 versus E curves such as those in Figure 5, once measured from the corresponding curve in the absence of the lipophilic ions, can be regarded as curves of $-(\beta - \alpha)\sigma'_i/\beta$ versus E. Moreover, in view of eq 5, the height ΔQ_0 of these curves can be regarded as a measure of $-(\beta - \alpha)\sigma_i/\beta$. Within the limits in which we may disregard α with respect to β, the curves of $-Q_0$ versus E can be taken as σ'_i versus E curves; hence their height measures directly the charge density σ_i of lipophilic ions adsorbed in the polar head region at E_i, while the plots in Figures 4, 6, and 8 are adsorption isotherms of these ions.

The Differential Capacity versus Potential Curves. A simple, albeit approximate, correlation between the C vs E curves and the corresponding chronocoulometric σ'_i versus E curves can be derived if in eq 1 the potential difference across the diffuse layer and the polar head region is neglected with respect to that across the hydrocarbon tail region:

$$\Psi_0 \cong \frac{4\pi\alpha}{\epsilon_1}\sigma_M + \frac{4\pi(\beta-\alpha)}{\epsilon_1}(\sigma_M + \sigma'_i) = \frac{4\pi\beta}{\epsilon_1}\sigma_M + \frac{4\pi(\beta-\alpha)}{\epsilon_1}\sigma'_i \quad (6)$$

Following Andersen and Fuchs,[3] we will assume that at equilibrium the ratio of the charge densities σ'_i and σ''_i in the two potential wells at $x = \alpha$ and $x = \beta$ is given by the Boltzmann relationship:

$$\frac{\sigma'_i}{\sigma''_i} = \exp\left[-\frac{zF}{RT}\frac{4\pi(\beta-\alpha)}{\epsilon_1}(\sigma_M + \sigma'_i) + \frac{U}{RT}\right] \quad (7)$$

where z is the valence of the lipophilic ion. The first term in the exponent is the difference in the electrostatic potential energy between the two wells in RT units, while the second term accounts for the difference U in the nonelectrostatic potential energy which exists in an asymmetrical lipid layer such as that under study. Let us assume once again that $\sigma'_i + \sigma''_i = \sigma_i$ is a constant. Upon substituting $\sigma''_i = \sigma_i - \sigma'_i$ in eq 7 and differentiating σ_M as derived from the resulting equation with respect to σ'_i, we obtain:

$$\frac{d\sigma_M}{d\sigma'_i} = -\frac{RT}{zF}\frac{\epsilon_1}{4\pi(\beta-\alpha)}\frac{\sigma_i}{\sigma'_i(\sigma_i - \sigma'_i)} - 1 \quad (8)$$

Differentiation of Ψ_0 in eq 6 with respect to σ_M yields the reciprocal of the differential capacity C:

$$\frac{1}{C} = \frac{d\Psi_0}{d\sigma_M} = \frac{1}{C_0} + \frac{4\pi(\beta-\alpha)}{\epsilon_1}\frac{d\sigma'_i}{d\sigma_M} \quad (9)$$

where $C_0 \equiv \epsilon_1/(4\pi\beta)$ is the differential capacity in the absence of the lipophilic ions. On substituting $d\sigma_M/d\sigma'_i$ from eq 8 into eq 9 and regarding α as negligible with respect to β as usual,

after rearrangement we obtain:

$$C = C_0 + \frac{zF}{RT}\frac{\sigma'_i(\sigma_i - \sigma'_i)}{\sigma_i} \quad (10)$$

It is readily seen from this equation that the maximum differential capacity is attained at the midpoint of the corresponding σ'_i versus E curve, namely, for $\sigma'_i = \sigma_i/2$.

The dashed curve in Figure 1A was calculated from eq 10 on the basis of the σ'_i versus E curve corresponding to the experimental C versus E curve a. While the hump of the experimental C versus E curve has approximately the same height as that of the corresponding calculated curve, its position relative to the potential axis is shifted in the negative direction. Conversely, the experimental C versus E curves for $TPhP^-$ adsorption in PS were found to be shifted toward positive potentials with respect to those calculated from eq 10. Summarizing, the experimental C versus E curves for both lipophilic ions are shifted in the direction of increasing translocation toward the mercury surface with respect to the curves calculated on the basis of the corresponding σ'_i versus E curves. This phenomenon must be ascribed to the progressive diffusion of the lipophilic ions from the bulk solution to the mercury surface during the recording of the differential capacity curves. Now, eq 10 predicts that the maximum height of these curves is attained when the charge density σ''_i in the polar head region is one-half of the corresponding equilibrium charge density σ_i before translocation. While in chronocoulometric measurements this situation is realized when the charge density σ'_i in direct contact with mercury is also equal to $\sigma''_i = \sigma_i/2$, in differential capacity measurements it is realized for $\sigma'_i > \sigma_i/2$ because of the gradual diffusion of the lipophilic ions toward the electrode. The resulting greater electrostatic repulsion exerted by σ'_i on the translocating ions in differential capacity measurements is responsible for the observed potential shift of the capacity humps with respect to the midpoint of the corresponding σ'_i versus E curves.

An Adsorption Isotherm Accounting for Discreteness of Charge Effects. The adsorption isotherms of $TPhP^+$ in a PS monolayer (see Figure 4) and of $TPhB^-$ in a PC monolayer (see Figure 8) show appreciable deviations from the Henry isotherm behavior, which are similar to those reported by other investigators for the $TPhB^-$ [5,6,24] and DpA^- anions.[4,5,24-26] In view of the low charge densities σ_i involved, it is improbable that these deviations may be ascribed to the saturation of a limited number of binding sites in the lipid monolayer. In fact, this monolayer can be contracted or expanded by more than 20% with a resulting change in its thickness but without any loss in its self-organization and in its impermeability to inorganic ions;[12] this implies that the polar head groups can be easily pushed aside by the adsorbing lipophilic ions, even though we cannot exclude a resulting small local disturbance in the conformation of these groups. Deviations from the Henry isotherm behavior are therefore expected to be mainly due to repulsive interactions. Andersen et al.[6] explained these deviations by writing the adsorption isotherm in the general form valid far from saturation:

$$|\sigma_i| = K_0 c \exp(-zF\psi/RT) \quad (11)$$

where K_0 is the adsorption coefficient for $\psi = 0$. Strictly speaking, ψ is the local electric potential (the so-called micropotential) at the position occupied by an adsorbed ion of charge ze, relative to the adjacent bathing solution. The adsorption coefficient K as obtained directly from the slope of $|\sigma_i|$ versus c plots over the Henry isotherm region is then given by:

$$K \equiv \lim_{\sigma_i \to 0}\left(\frac{|\sigma_i|}{c}\right) = K_0 \exp\left[-\frac{zF\psi(\sigma_i=0)}{RT}\right] \quad (12)$$

Andersen et al.[6] identified ψ with the corresponding average potential Ψ (the macropotential) for simplicity; the latter potential was therefore set equal to the average potential difference across the burial depth γ plus the potential difference Ψ_d across the diffuse layer as estimated by the linearized Gouy–Chapman theory. In interpreting the adsorption isotherms of DpA^- in PC bilayers at different ionic strengths, Wang and Bruner[7] also used eq 11, setting ψ equal to Ψ_d. In interpreting surface potential measurements on PE monolayers in the presence of $TPhP^+$ ions, Andersen et al.[6] felt the need to account for discreteness-of-charge effects by using an expression for the micropotential ψ in eq 11; this was obtained by regarding the adsorbed anions as arranged in a fixed hexagonal array and by including the effect of their images in the $x = d$ plane (O–C imaging according to Barlow and MacDonald's notations[27]). Tsien and Hladky[28] reexamined the adsorption isotherm of $TPhB^-$ in PE bilayers as determined by Andersen et al.[6] in the light of a virial isotherm[29] in which the potential energy of interaction between a pair of adsorbed ions was estimated by including the effect of their infinite images in the surfaces separating the bilayer from the two bathing solutions. Wang and Bruner[30] considered the single imaging of the DpA^- anions adsorbed on one side of a PC bilayer in the surface $x = d$ separating that side from the adjacent bathing solution to explain the increase in the relaxation time for transient current flow across this bilayer with an increase in the bulk DpA^- concentration. To this end the charge density σ_i of the adsorbed DpA^- anions around a given anion was assumed to be smeared out uniformly on the adsorption plane except for a charge-free disk of constant radius a (the so-called exclusion or cut-off disk) with center in the position of the given anion; the effect of the single image of this disk in the $x = d$ plane was accounted for.

All the above treatments accounting for discreteness-of-charge effects represent lipid monolayers or bilayers as slabs of uniform dielectric constant ϵ, and hence neglect one important feature of these layers, namely, the presence of a hydrocarbon tail region, with a dielectric constant $\epsilon_1 \approx 2$, and of a polar head region, with a dielectric constant ϵ_2 ranging from 8 to 50.[31] Moreover, they completely disregard the effect of the potential difference Ψ_d across the diffuse layer. This may explain why fitting the predictions of these different models to experimental adsorption isotherms leads to quite different values for the single dielectric constant ϵ and for the burial depth γ. Thus, in the "hexagonal array model" adopted by Andersen et al.,[6] the parameters ϵ and γ were given the values 10 and 8 Å. Conversely, in the virial isotherm by Tsien and Hladky,[28] ϵ was set equal to 2.1 and γ was given values ranging from 1.5 to 2.5 Å. A still lower γ value, 0.5 Å, almost negligible with respect to the thickness of the polar head region, was employed by Wang and Bruner[30] in their "cutt-off disk model" to fix experimental relaxation times. This scattering in ϵ and γ values reflects the different particular features emphasized by the different models.

The expressions for the micropotential ψ reported in the Appendix (eq A4 with ϕ_a given by eq A3 and the limiting expression of eq A6) refer to the model of Figure 10 that was used to estimate the experimental adsorption isotherms. Thus they account for the presence of two distinct regions of dielectric constant ϵ_1 and ϵ_2 and thickness β and γ, respectively. The electrode surface plane $x = 0$ and the membrane/solution

boundary $x = d$ are treated as perfect conductors (perfect C−C imaging according to Barlow and MacDonald's notations[27]). Discreteness-of-charge effects are considered in the framework of the "cutt-off disk model", according to which an adsorbed ion is surrounded by a charge-free disk that is imaged infinite times in the $x = 0$ and $x = d$ planes. The expected values for the parameters of a typical lipid monolayer are 10−20 Å for β, 4−10 Å for γ, ≈2 for ϵ_1, and 8−50 for ϵ_2.[31] Moreover, large lipophilic ions have radii of the order of 3−5 Å, and hence the "steric hard-core radius" between two neighboring ions is of the order of 6−10 Å. The exclusion disk radius a cannot be smaller than this steric hard-core radius. With these parameters, eq A4 yields absolute values for the micropotential ψ that are close to the minimum "limiting values" furnished by eq A6, which holds for $a \rightarrow \infty$. In other words, when a is comparable with the distance 2γ between the adsorbed charges and their nearest-neighboring images, the screening effect of these images becomes so large as to cause the limiting behavior for $a \rightarrow \infty$ to be closely approached. In the Appendix it is shown that the expression for ψ of eq A6 is rigorous and represents the limiting case for $a \rightarrow \infty$ not only in the framework of the "cutt-off disk model", but also in that of the "hexagonal array model". On the contrary, eqs A3 and A4, albeit more general, are approximate, and their accuracy decreases with increasing a. In practice, on using β, γ, ϵ_1, and ϵ_2 values typical of lipid layers and steric hard-core radii a typical of lipophilic ions, the ψ values obtained from eqs A3 and A4 become erroneously lower than the corresponding minimum limiting values obtained from eq A6. Hence, in the following only the limiting expression of eq A6 will be employed.

It is interesting to estimate the "Coulombic hard-core radius" a_c, namely, the distance of closest approach between two adsorbed ions resulting from their mutual Coulombic repulsion. This radius, which depends on the screening conditions, can be estimated from the expression:[32]

$$\pi a_c^2 = \int_0^\infty \{1 - \exp[-zF\phi(\varrho)/RT]\} 2\pi\varrho \, d\varrho \qquad (13)$$

where $\phi(\varrho)$ is the potential created by one adsorbed ion and by its infinite regress of images at a distance ϱ on the adsorption plane $x = \beta$. An approximate expression for $\phi(\varrho)$ is provided by eq A1; however, this expression becomes inaccurate when $\phi(\varrho)$ becomes very low on account of the progressive increase in ϱ, such as to provide unphysical $\phi(\varrho)$ values of opposite sign with respect to the ion generating the potential. Fortunately enough, at these high ϱ values the potential turns out to depend practically on the two ratios β/ϵ_1 and γ/ϵ_2 rather than on the four separate parameters β, γ, ϵ_1, and ϵ_2 (see Appendix). Hence the low $\phi(\varrho)$ values were calculated from eq A1 by forcing ϵ_1 and ϵ_2 to become equal while changing either β or γ in order to keep the β/ϵ_1 and γ/ϵ_2 ratios constant; in fact, eq A1 becomes rigorous for $\epsilon_1 = \epsilon_2$. Setting $\beta = 20$ Å and $\epsilon_1 = 2$, numerical integration of eq 13 yields $a_c = 7.5$ Å for $\gamma = 4$ Å and $\epsilon_2 = 30$, and $a_c = 23.5$ Å for $\gamma = 10$ Å and $\epsilon_2 = 8$. The first value for the Coulombic hard-core radius corresponds to a limiting situation of high screening (low γ and high ϵ_2) and is comparable with the "steric hard-core radius". Conversely the second a_c value corresponds to a limiting situation of low screening (high γ and low ϵ_2).

If we substitute the limiting expression for ψ of eq A6 into the general isotherm of eq 11, we obtain:

$$\ln\left(\frac{|\sigma_i|}{c}\right) = \ln K_0 - \frac{zF}{RT}\left[\frac{4\pi\gamma}{\epsilon_2}\left(\sigma_M + \sigma_i \frac{\gamma/\epsilon_2}{\gamma/\epsilon_2 + \beta/\epsilon_1}\right) + \Psi_d\right] \qquad (14)$$

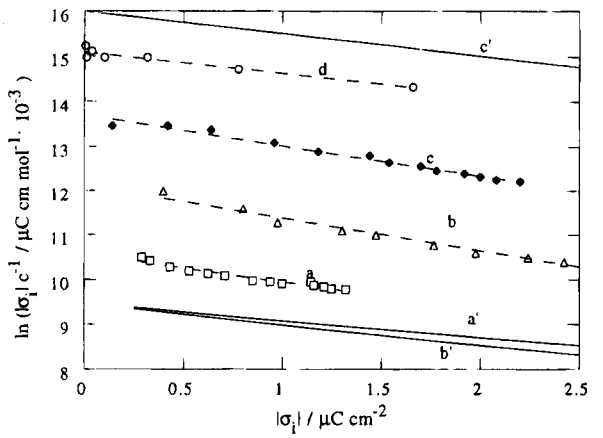

Figure 11. $\ln(|\sigma_i|c^{-1})$ vs $|\sigma_i|$ plots for $TPhP^+$ in a PS monolayer in contact with pH 3 (a) and pH 9 (b) buffered solutions of 0.1 M KCl, for $TPhB^-$ in a PC monolayer in contact with an unbuffered solution of 0.1 M KCl (c) and for $TPhB^-$ in a PE bilayer in contact with 1 M NaCl (d).[6] The solid curves a′ and b′ were calculated from eq 14 for a lipid monolayer by setting $\beta/\epsilon_1 = 10$ Å and equating γ/ϵ_2 to 1.25 and 0.133 Å, respectively, whereas curve c′ was calculated from eq 16 for a lipid bilayer by setting $\beta/\epsilon_1 = 10$ Å and $\gamma/\epsilon_2 = 1.25$ Å. The position of the calculated curves a′, b′, and c′ along the vertical axis is arbitrary. The slopes of these curves are −0.62 (a), −0.73 (b), −0.68 (c), −0.46 (d), −0.38 (a′), −0.46 (b′), and −0.48 cm^2 μC^{-1} (c′). See text for details.

which depends on the parameters of the lipid layer only through the β/ϵ_1 and γ/ϵ_2 ratios. If the charge density σ_h of the polar heads of the lipid is different from zero and we may assume that its burial depth is equal to γ, then σ_i must be replaced by $(\sigma_i + \sigma_h)$ both in this equation and in the following eq 16. Within the limits in which σ_M and Ψ_d vary only slightly with varying σ_i, the adsorption isotherm of eq 14 has the same form as the truncated virial isotherm[28] or also the isotherm proposed by Andersen et al.[6] on the basis of their three-capacitor model; moreover, it predicts a linear slope for the $\ln(|\sigma_i|c^{-1})$ versus σ_i plot.

Comparison of the Proposed Adsorption Isotherm with Experiment. In view of the isotherm of eq 14, we have found it convenient to report our experimental data for $TPhB^-$ and $TPhP^+$ adsorption in PC and PS monolayers in the form of $\ln(|\sigma_i|c^{-1})$ versus $|\sigma_i|$ plots (see Figure 11). It is apparent that these plots are actually roughly linear, with slopes ranging from about −0.4 to about −0.7 cm^2 μC^{-1}. The solid curves a′ and b′ in Figure 11 are plots calculated from eq 14 by setting $\beta/\epsilon_1 = 20$ Å/2 and ascribing to γ/ϵ_2 the extreme values 10 Å/8 and 4 Å/30. The position of these plots along the vertical axis is arbitrary, since the theoretical isotherm of eq 14 predicts deviations of experimental σ_i versus c curves from linear behavior, but not the initial slope $K_0 \exp[-zF\psi(\sigma_i=0)/RT]$ of these curves, and hence the intercept, $\ln K_0 - [zF\psi(\sigma_i=0)/RT]$, of the $\ln(|\sigma_i|c^{-1})$ versus $|\sigma_i|$ plots on the vertical axis. The calculated curves a′ and b′ in Figure 11 refer to $TPhB^-$ adsorption in the neutral lipid PC at an applied potential $E_i = -0.75$ V. The dependence of σ_M on σ_i was estimated by considering that the average potential difference Ψ_0 across the whole interphase is given by:

$$\Psi_0 = \frac{4\pi\beta}{\epsilon_1}\sigma_M + \frac{4\pi\gamma}{\epsilon_2}(\sigma_M + \sigma_i) + \chi + \Psi_d \qquad (15)$$

where χ is the surface dipole potential. The Ψ_0 value is not experimentally accessible, but differs from the applied potential E_i by a constant which depends exclusively upon the choice of the reference electrode; hence, Ψ_0 is constant at constant E_i. If we assume that χ remains approximately constant at constant

E_i with varying the experimental conditions and we use the Gouy–Chapman theory to estimate Ψ_d, independent measurements of σ_M (in preparation) carried out in the absence of lipophilic ions (i.e., for $\sigma_i = 0$) permit us to ascribe a value of about −0.75 V to the quantity $(\Psi_0 - \chi)$ at $E_i = -0.750$ V by using eq 15 in which $4\pi(\beta/\epsilon_1 + \gamma/\epsilon_2)$ is equated to the reciprocal of the experimental differential capacity $C \approx 1.7$ μF cm^{-2} as a first approximation. Equation 15, with Ψ_d expressed as a function of $(\sigma_M + \sigma_i)$ and c on the basis of the Gouy–Chapman theory, is an implicit function of σ_M, from which σ_M is readily calculated for each σ_i value by using the Newton–Raphson iterative procedure. The calculated curves a′ and b′ in Figure 9 are practically linear with an average slope of −0.38 cm^2 μC^{-1} for $\gamma/\epsilon_2 = 1.25$ Å and −0.46 cm^2 μC^{-1} for $\gamma/\epsilon_2 = 0.133$ Å. It is apparent that these slopes are scarcely sensitive to changes in the values of the parameters for the lipid monolayer. This is due to the fact that a change in σ_i at constant applied potential E_i is accompanied by a change in σ_M in the opposite direction, such that the first term between square brackets in eq 14 becomes relatively negligible with respect to Ψ_d.

Equation 14 can also be applied to lipid bilayers as a good approximation. In fact, the distance, $\approx 2\beta$, of the ions adsorbed on one side of the membrane from those adsorbed on the other side together with their diffuse-layer counterions is large with respect to the distance, γ, from the solution bathing the same side; this may permit us to regard the overall charge on the other side of the membrane, including the diffuse-layer counterions, as approximately located on the relative membrane surface. In the available literature, adsorption measurements have been generally carried out on symmetrical bilayers starting from an initially zero transmembrane potential. Under these conditions the overall charge on the other side of the membrane equals zero; hence, eq 14 can be directly applied to these bilayers by setting $\sigma_M = 0$ and by substituting β with 2β:

$$\ln|\sigma_i| + \frac{zF}{RT}\left[4\pi\sigma_i\frac{(\gamma/\epsilon_2)^2}{\gamma/\epsilon_2 + 2\beta/\epsilon_1} + \Psi_d\right] = \ln K_0 + \ln c \quad (16)$$

Curve d in Figure 11 shows the experimental $\ln(|\sigma_i|c^{-1})$ versus $|\sigma_i|$ plot as obtained from the isotherm for $TPhB^-$ adsorption in a PE bilayer from 1 M NaCl.[6] The slope of this plot, −0.46 cm^2 μC^{-1}, is close to the slope, −0.48 cm^2 μC^{-1}, of the solid curve c′ in the same figure, calculated from eq 16 by setting $\beta/\epsilon_1 = 10$ Å and $\gamma/\epsilon_2 = 1.25$ Å and by estimating Ψ_d from the Gouy–Chapman theory for a 1 M 1,1-valent electrolyte.

The points in Figure 12 are data by Wang and Bruner[7] for DpA^- adsorption in a PC bilayer from NaCl solutions of different concentrations. The solid curves in this figure are plots of log $|\sigma_i|$ versus (log c + constant) calculated from eq 16 for the same electrolyte concentrations using the same parameters as in curve c′ of Figure 11; the whole set of calculated curves was shifted along the log c axis to achieve the best overlapping with the experimental points. Agreement is fairly good. At the lowest electrolyte concentrations, the ionic surface potential Ψ_d prevails decidedly over the first term between square brackets in eq 16, $4\pi\sigma_i(\gamma/\epsilon_2)^2/(\gamma/\epsilon_2 + 2\beta/\epsilon_1)$, which accounts for the presence of a burial depth γ via the average potential contribution $4\pi\sigma_i(\gamma/\epsilon_2)$ times the $(\gamma/\epsilon_2)/(\gamma/\epsilon_2 + 2\beta/\epsilon_1)$ factor accounting for discreteness-of-charge effects. This explains why Wang and Bruner[7] were able to ascribe the whole repulsive effect to Ψ_d at the lowest electrolyte concentrations. However, an increase in the electrolyte concentration causes Ψ_d to become comparable and ultimately small with respect to the first term in eq 16; this forced Wang and Bruner[7] to use fictituously low values for the dielectric constant in the Gouy–Chapman expression for Ψ_d, thus postulating a dielectric saturation of the aqueous solution adjacent to the bilayer. It should be noted that the experimental repulsive effect being greater than predicted on the basis of the simple Ψ_d potential cannot be satisfactorily accounted for by adding to Ψ_d the sole average potential difference $4\pi\sigma_i(\gamma/\epsilon_2)$, unless the burial depth γ is ascribed unphysically low values. This shows that both the diffuse-layer contribution and discreteness-of-charge effects must be considered in order to justify the experimental behavior on the basis of realistic parameters for the lipid layer.

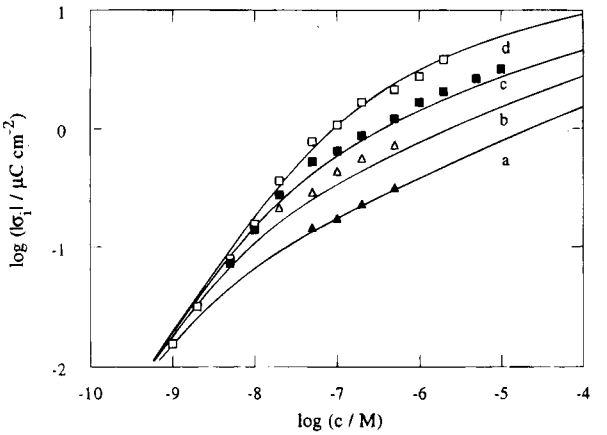

Figure 12. Points are log($|\sigma_i|$) values against log c for DpA^- adsorption in a PC bilayer from 1×10^{-4} (a), 1×10^{-3} (b), 1×10^{-2} (c), and 1 M NaCl (d).[7] The solid curves are plots calculated from eq 16 for $\beta/\epsilon_1 = 10$ Å and $\gamma/\epsilon_2 = 1.25$ Å.

The pH Dependence of Ionic Adsorption in Phosphatidylserine Monolayers. The initial linear portion of the adsorption isotherm of $TPhP^+$ cations in a PS monolayer exhibits an apparently anomalous behavior with varying pH (see Figure 9). Clearly, over this linear portion the progressive electrostatic repulsion between the adsorbing $TPhP^+$ cations following an increase in their charge density σ_i is still negligible. However, the electrostatic interaction of these cations with the charge density σ_h of the polar heads of PS must be taken into account and is responsible for the change in the slope, K, of the Henry isotherm region with a change in pH. The interaction between the adsorbed ions and σ_h is readily accounted for by substituting σ_i with $(\sigma_i + \sigma_h)$ on the right-hand side of the adsorption isotherm of eq 14. Using the protonation constants of the phosphate and carboxyl groups for a PS monolayer as estimated from differential capacity measurements[12] and calculating Ψ_d as a function of $(\sigma_M + \sigma_h)$ and of the electrolyte concentration on the basis of the Gouy–Chapman theory, eq 14 with $\sigma_i = 0$, $\beta/\epsilon_1 = 10$ Å, and $\gamma/\epsilon_2 = 0.133$ Å yields the curve of $-F\psi(\sigma_i{=}0)/RT$ = (ln K + constant) against pH in Figure 9.

PS monolayers deposited on mercury in the absence of incorporated species were found to bear a charge density σ_h passing from a small positive value of about +4 μC cm^{-2} at pH 3 to a small negative value of about −3 μC cm^{-2} at pH 9.[12] As a consequence, in the neighborhood of pH 6, where PS is electrically neutral, the calculated curve of $-F\psi(\sigma_i{=}0)/RT$ versus pH shows a plateau region interposed between a downswing at low pH values and an upswing at high pH values. This calculated curve contrasts with the experimental curve, which shows a maximum slope just at pH 6. This behavior is consistent with the conclusions drawn in ref 12, according to which self-organized films of PS may assume at least two different conformations of the polar head with similar Gibbs energies, but quite different acidities of the ionizable groups.

When an increase in pH causes the PS monolayer to approach neutrality, the presence of an adsorbed lipophilic cation will tend to favor the conformation with a negatively charged phosphate group in the nearest neighboring polar heads. The experimental ln K versus pH plot in Figure 9 exhibits a relatively abrupt increase of 0.5 over the pH range from 5 to 6; this increase is equal to the contribution, $-F\phi(\varrho)/RT$, from the electrostatic potential created at the position of a $TPhP^+$ cation adsorbed on the $x = \beta$ plane by a monovalent anion on the same plane at a distance $\varrho = 7.4$ Å and by its infinite regress of images, as estimated from eq A1 for $\beta = 20$ Å, $\gamma = 4$ Å, $\epsilon_1 = 2$, and $\epsilon_2 = 30$. We may therefore postulate that over the Henry isotherm region the presence of an adsorbed $TPhP^+$ cation induces a conformational change in one neighboring PS polar head, leading to a deprotonation of its phosphate group.

The progressive increase in the negative charge density σ_h of the PS polar heads with an increase in pH beyond 6 is expected to have a relatively small effect on the micropotential ψ at the position of an adsorbed $TPhP^+$ cation, when compared with the effect already produced between pH 5 and 6 by one negative polar head immediately adjacent to the given cation. Nonetheless, this cannot entirely justify the modest increase in ln K with an increase in pH beyond 6 as compared with that predicted by eq 14. At any rate, independent measurements of σ_M and of the differential capacity on PS monolayers deposited on mercury (Moncelli, Becucci, and Guidelli, unpublished results) seem to indicate an appreciable positive shift in the surface dipole potential χ with an increase in pH beyond 6, which may oppose a rapid increase in $TPhP^+$ adsorptivity.

The progressively positive charge density σ_h assumed by the PS polar heads with decreasing pH below 6 is expected to have a minor effect on ψ, because the burial depth of the positively charged amino groups is almost certainly smaller than that of the phosphate groups, and hence their charge is much more effectively screened by the water molecules and by the diffuse-layer ions of the bathing solution. This may also explain the lack of an appreciable increase in ln K for $TPhB^-$ adsorption in PS with a decrease in pH below 6 (see curve b in Figure 9). These lipophilic anions do not even show an appreciable decrease in ln K with an increase in the negative charge density σ_h following an increase in pH beyond 6. This may be due, at least partially, to the tendency of the $TPhB^-$ anions to impose a neutral conformation, with a protonated phosphate group, on the nearest neighboring PS polar heads, even when their mean charge density σ_h approaches a value of $-3\ \mu C\ cm^{-2}$. A further effect in this direction may also be produced by a positive shift of χ with an increase in pH.

The notably asymmetric electrostatic effect exerted by the PS polar heads on the structurally very similar, but oppositely charged, $TPhP^+$ and $TPhB^-$ ions casts some doubt on the validity of the use of lipophilic ions as probes of the charge density or of the ionic surface potential Ψ_d at membranes containing PS molecules. In fact, these ions experience a local electric potential which they contribute to alter appreciably even when their concentration inside the membrane is very low.

Acknowledgment. The authors wish to thank Mr. Luciano Righeschi for valuable technical assistance. Thanks are due to the Ministerio de Educatión y Ciencia of Spain for a fellowship to R.H. during the tenure of which most of the present results were obtained. The financial support of the Ministero dell'Universita' e della Ricerca Scientifica e Tecnologica and of the Consiglio Nazionale delle Ricerche is gratefully acknowledged.

Appendix

The two most popular models employed to account for discreteness-of-charge effects are the hexagonal lattice model and the cut-off disk model. In the hexagonal lattice model the ions are arranged in a fixed hexagonal array, i.e., the two-dimensional structure which minimizes the interaction energy of the ions. In the cutt-off disk model, an ion is surrounded by a circular charge-free region, called the exclusion disk; beyond the cut-off radius, the charge is taken as smeared out uniformly. Of the possible types of imaging, we will choose the perfect "conducting-conducting" imaging conditions; namely, we will assume that both the metal surface plane, $x = 0$, and the lipid monolayer/solution boundary, $x = d$, act as perfect conductors. In a series of papers, Levine et al.[32-36] accounted for the screening effect of the diffuse layer in treating discreteness-of-charge effects, but the approximations underlying their approach are inapplicable under the present experimental conditions. In fact, in Levine's approach the effect of an adsorbed discrete ion upon the neighboring diffuse layer ions is treated as a small perturbation in the solution of the Poisson–Boltzmann equation. Conversely, at electrolyte concentrations ≥ 0.1 M, the Debye length is <10 Å, and hence is smaller than the distance of closest approach between two bulky adsorbed lipophilic ions. The roughly hemispherical ionic cloud induced by an adsorbed ion will therefore hardly overlap with that of the neighboring adsorbed ions, and the free energy involved in the replacement of this hemispherical ionic cloud by the Debye–Hückel ionic atmosphere upon removal of the ion from the adsorbed state will not be affected by mutual interactions between the adsorbed ions. In other words, this free energy change will affect the value of the adsorption coefficient of the ion, but not the deviations of the adsorption isotherm from the Henry isotherm behavior. Under these conditions, Levine's correction for diffuse-layer screening does not necessarily represent an improvement, but it may lead to erroneous results. Thus, the imaging due to the presence of a plane $x = d$ of dielectric discontinuity (dielectric imaging) is not superimposable on the conductive imaging due to the presence of the diffuse layer ions; given one imaging mode at a certain level, the other mode will adjust its level so that the total effect is no more than perfect imaging.[27]

The results of the cut-off disk model depend crucially upon the choice of the cut-off radius a. If this radius is exclusively determined by steric hard-core repulsions, then it is independent of the charge density σ_i of the adsorbed ions and is of the order of 6–10 Å in the case of large lipophilic ions. If a is determined by the Coulombic repulsion between ion pairs, then it is still independent of σ_i in the case of perfect conducting-conducting imaging, but it may turn out to be larger than the "steric hard-core" radius. Finally, the cut-off disk area, πa^2, can be equated to the mean area occupied by one adsorbed ion, ze/σ_i, where z is the valence of the ion and e is the absolute value of the electron charge.[33] In this case, a is clearly dependent on σ_i and yields results close to those of the hexagonal lattice model. The relation between a and the lattice constant s of the hexagonal lattice model is obtained by equating πa^2 to the area allotted to each ion in the hexagonal array, $(3^{1/2}/2)s^2$; hence, $a = 0.525$ s. The hexagonal lattice model (or, which is equivalent, the cutt-off disk model with $a = (ze/\pi\sigma_i)^{1/2}$) is generally considered to overestimate the order, the hence to underestimate electrostatic repulsions, for charge densities less than about 9 $\mu C\ cm^{-2}$.[27] A less ordered model, such as a cut-off disk model with constant a, seems therefore more appropriate for the low charge densities (usually $<3\ \mu C\ cm^{-2}$) typical of lipophilic ions adsorbed in membranes. At any rate, in what follows it will

be shown that the problem of the choice of the cut-off radius, whether constant or σ_i dependent, is notably simplified in the case of lipid monolayers or bilayers.

An important feature which has been so far neglected in treating discreteness-of-charge effects in lipid layers is the presence of two regions of appreciably different dielectric constants: the hydrocarbon tail region, with a dielectric constant $\epsilon_1 \approx 2$, and the polar head region, with an effective dielectric constant ϵ_2 ranging from 8 to 50.[31] Adsorbed lipophilic ions are buried in the polar head region, with a burial depth of the order of magnitude of the thickness of this region, which ranges from 4 to 10 Å. As a first approximation we may locate the position of the adsorbed ions at the boundary between the two regions of different dielectric constant. Let us regard once again a lipid monolayer deposited on mercury as consisting of a hydrocarbon tail region of dielectric constant ϵ_1 enclosed between the electrode surface plane $x = 0$ and the plane $x = \beta$, and of a polar head region of dielectric constant ϵ_2 enclosed between $x = \beta$ and the lipid/solution boundary $x = d = \beta + \gamma$ (see Figure 10). We will further assume perfect conducting-conducting imaging in the $x = 0$ and $x = d$ planes. Consider a charge ze located at $x = \beta$; an approximate expression for the potential created by this charge and by its infinite regress of images at a distance ϱ on the same $x = \beta$ plane was provided by Levine and Robinson.[36]

$$\phi(\varrho) = \frac{4ze}{d(\epsilon_1 + \epsilon_2)}\left\{\sum_{n=1}^{\infty}[a_n K_0(nR)] - \frac{\epsilon_2 - \epsilon_1}{\pi(\epsilon_2 + \epsilon_1)}\sum_{n=1}^{\infty}[c_n K_0(nR) + d_n R K_1(nR)]\right\} \quad \text{(A1)}$$

with

$$R \equiv \frac{\pi\varrho}{d}; \quad B \equiv \frac{\pi\beta}{d}; \quad \Gamma \equiv \frac{\pi\gamma}{d}; \quad a_n \equiv 1 - \cos(2nB)$$

$$c_n \equiv (B - \Gamma)[\cos(2n\Gamma) - \cos(4nB)];$$

$$d_n \equiv \sin(2n\Gamma) + {}^1/_2 \sin(4nB) \quad \text{(A2)}$$

Here K_n is the Bessel function of the second kind with imaginary argument and of order n. This equation was obtained by expanding the rigorous expression of $\phi(\varrho)$ in a power series of $(\epsilon_2 - \epsilon_1)/(\epsilon_2 + \epsilon_1)$ and arresting the expansion at the linear term. When we have either $\epsilon_1 = \epsilon_2$ (and $\beta \neq \gamma$) or $\beta = \gamma$ (and $\epsilon_1 \neq \epsilon_2$), then the second term between braces in eq A1 vanishes and the resulting expression becomes rigorous. Otherwise, the accuracy of eq A1 decreases with an increase of ϱ with respect to β and γ.

The electric potential ϕ_a which a disk of uniform charge density $-\sigma_i$ and radius a located on the $x = \beta$ plane and its infinite regress of images in $x = 0$ and $x = d$ create just at the center of the disk, is expressed by:[36]

$$\phi_a = -\frac{8d\sigma_i}{\pi(\epsilon_1 + \epsilon_2)}\left\{B\Gamma - A\sum_{n=1}^{\infty}\frac{a_n}{n}K_1(nA) + \frac{\epsilon_2 - \epsilon_1}{\pi(\epsilon_2 + \epsilon_1)}\left[B(B - \Gamma)(2B - \Gamma) - \frac{2\pi^3}{3} + 2\pi(2B^2 + \Gamma^2) - \frac{4}{3}(4B^3 + \Gamma^3) + A\sum_{n=1}^{\infty}\left(\frac{c_n}{n} + \frac{2}{n^2}d_n\right)K_1(nA) + A^2\sum_{n=1}^{\infty}\frac{d_n}{n}K_0(nA)\right]\right\} \quad \text{(A3)}$$

with $A \equiv \pi a/d$. This expression for the "disk potential" ϕ_a has about the same degree of accuracy as eq A1 and becomes likewise rigorous for $\epsilon_1 = \epsilon_2$ or for $\beta = \gamma$, namely, when the linear term in $(\epsilon_2 - \epsilon_1)/(\epsilon_2 + \epsilon_1)$ vanishes. The disk potential is the potential which must be added to the uniform charge distribution σ_i on the $x = \beta$ plane and to its infinite images to produce charge-free circular holes of radius a on all these planes; hence, it is the correction which must be made to the average potential Ψ (the so-called macropotential) to account for the local perturbation produced by the charge ze and to obtain the local potential ψ (the so-called micropotential) at the position occupied by this charge relative to the bulk solution. The infinite images of the uniform charge distribution σ_i on the $x = \beta$ plane have no effect on the dielectric slab enclosed between the two conducting planes $x = 0$ and $x = d$, because they have alternatively charge densities σ_i and $-\sigma_i$, and hence their electric fields cancel each other within the slab; consequently, the macropotential which must be added to ϕ_a to obtain the micropotential is that produced by the charge distribution σ_i on the $x = \beta$ plane, plus that produced by the charge density σ_M on the metal surface plane and by the charge of the diffuse-layer ions. In view of Gauss's law and the Gouy–Chapman theory, we have:

$$\psi = \Psi + \phi_a = \frac{4\pi\gamma}{\epsilon_2}(\sigma_M + \sigma_i) + \Psi_d + \phi_a \quad \text{(A4)}$$

where Ψ_d is the ionic surface potential as expressed by the Gouy–Chapman theory and ϕ_a is expressed by eq A3.

The expression of eq A3 for ϕ_a becomes progressively less accurate as the disk radius a increases with respect to β and γ. Fortunately, the minimum limiting value of ϕ_a for $a \to \infty$ is available:[35]

$$\phi_a = -4\pi\frac{(\beta/\epsilon_1)(\gamma/\epsilon_2)}{\gamma/\epsilon_2 + \beta/\epsilon_1}\sigma_i = -4\pi\frac{\beta\gamma}{\epsilon_1\gamma + \epsilon_2\beta}\sigma_i \quad \text{(A5)}$$

This expression can be readily justified on the basis of the same model of dielectric slab adopted by Levine et al.[32] for the particular case of $\epsilon_1 = \epsilon_2$. To this end consider those conditions for the imaging of the disk of infinite radius and charge density $-\sigma_i$ in the two planes $x = 0$ and $x = d$ which ensure the equipotentiality of these two planes. These conditions are satisfied if the disk on the $x = \beta$ plane is regarded as having two sides; the side turned toward the metal surface plane $x = 0$ is imaged there and has a charge density $-\sigma_i(\gamma/\epsilon_2)/(\gamma/\epsilon_2 + \beta/\epsilon_1)$, whereas the side turned toward the $x = d$ plane has a charge density $-\sigma_i(\beta/\epsilon_1)/(\gamma/\epsilon_2 + \beta/\epsilon_1)$ and is imaged in the latter plane. With these imaging conditions the electric field between the $x = 0$ and $x = \beta$ planes is $4\pi\sigma_i(\gamma/\epsilon_2)/[\epsilon_1(\gamma/\epsilon_2 + \beta/\epsilon_1)]$, and hence the potential difference between these two planes is $4\pi\sigma_i(\gamma/\epsilon_2)(\beta/\epsilon_1)/(\gamma/\epsilon_2 + \beta/\epsilon_1)$. Analogously, the electric field between the $x = \beta$ and $x = d$ planes is $-4\pi\sigma_i(\beta/\epsilon_1)/[\epsilon_2(\gamma/\epsilon_2 + \beta/\epsilon_1)]$, and hence the potential difference between them is $-4\pi\sigma_i(\gamma/\epsilon_2)(\beta/\epsilon_1)/(\gamma/\epsilon_2 + \beta/\epsilon_1)$, which is exactly the result of eq A5. Note that the limiting expression of eq A5 for the disk potential difference between $x = \beta$ and $x = d$ does not depend on the four distinct parameters β, γ, ϵ_1, and ϵ_2, but only on the two ratios β/ϵ_1 and γ/ϵ_2. From eq A4 it follows that the limiting expression of the micropotential ψ for $a \to \infty$ is:

$$\psi = \frac{4\pi\gamma}{\epsilon_2}\left(\sigma_M + \sigma_i\frac{\epsilon_1\gamma}{\epsilon_1\gamma + \epsilon_2\beta}\right) + \Psi_d \quad \text{(A6)}$$

It is interesting to note that the same limiting expression for ψ is obtained with the hexagonal lattice model. In this case the potential ψ_h created at the position of an adsorbed ion by all other ions of the hexagonal lattice and by their infinite images is given by:

$$\psi_h = \sum_{h=-\infty}^{+\infty} \sum_{k=-\infty}^{+\infty} \phi(\varrho) \qquad \text{(A7)}$$

with

$$\varrho = \sqrt{(hs + 0.5ks)^2 + (0.866ks)^2}$$

and $\phi(\varrho)$ expressed by eq A1. Here s is the lattice constant and the integers h and k run over all sites of the hexagonal array, except for the central site ($h = 0$, $k = 0$). The micropotential ψ is obtained by adding to ψ_h the contribution from the average potential difference arising from the charge σ_M on the metal surface plane and from that of the diffuse-layer ions. However, this contribution is now different from that of eq A4 for the cut-off disk model. The images of the charges of the hexagonal lattice, besides creating the appropriate electric field within the dielectric slab, cause the two imaging planes $x = 0$ and $x = d$ to be equipotential. In fact, when considering the whole set of charges on the $x = \beta$ plane together with their images, it is apparent that each charge has an opposite charge in a specular position with respect to both the $x = 0$ and the $x = d$ planes. A fraction σ'_M of the charge σ_M on the metal must therefore be used to ensure the equipotentiality of the $x = 0$ and $x = d$ planes due to the fictitious images.[27] In view of Gauss's law the potential difference between $x = 0$ and $x = d$ equals $4\pi[\beta\sigma_M/\epsilon_1 + \gamma(\sigma_M + \sigma_i)/\epsilon_2]$, and the charge σ'_M which causes this potential difference to vanish equals $-(\epsilon_1\gamma)\sigma_i/(\epsilon_1\gamma + \epsilon_2\beta)$. The average potential difference between the $x = \beta$ and $x = d$ planes is therefore produced by the excess charge $(\sigma_M - \sigma'_M)$, and the micropotential ψ relative to the bulk solution is obtained by adding ψ_h and Ψ_d to this average potential:

$$\psi = \frac{4\pi\gamma}{\epsilon_2}(\sigma_M - \sigma'_M) + \psi_h + \Psi_d = \frac{4\pi\gamma}{\epsilon_2}\left(\sigma_M + \sigma_i\frac{\epsilon_1\gamma}{\epsilon_1\gamma + \epsilon_2\beta}\right) + \psi_h + \Psi_d \qquad \text{(A8)}$$

Letting the disk radius a in the cut-off disk model tend to infinity amounts to letting the potential ψ_h tend to zero. Hence, in the low density limit, eq A8 becomes identical with the limiting expression of eq A6 for the cut-off disk model.

References and Notes

(1) Ketterer, B.; Neumcke, B.; Läuger, P. *J. Membr. Biol.* **1971**, *5*, 225–245.
(2) Hall, J. E.; Mead, C. A.; Szabo, G. *J. Membr. Biol.* **1973**, *11*, 75–97.
(3) Andersen, O. S.; Fuchs, M. *Biophys. J.* **1975**, *15*, 795–830.
(4) Bruner, L. J. *J. Membr. Biol.* **1975**, *22*, 125–141.
(5) Benz, R.; Läuger, P.; Janko, K. *Biochim. Biophys. Acta* **1976**, *455*, 701–720.
(6) Andersen, O. S.; Feldberg, S.; Nakadomari, H.; Levy, S.; McLaughlin, S. *Biophys. J.* **1978**, *21*, 35–70.
(7) Wang, C. C.; Bruner, L. J. *J. Membr. Biol.* **1978**, *38*, 311–331.
(8) Läuger, P.; Benz, R.; Stark, G.; Bamberg, E.; Jordan, P. C.; Fahr, A.; Brock, W. *Q. Rev. Biophys.* **1981**, *14*, 513–598.
(9) Brock, W.; Stark, G.; Jordan, P. C. *Biophys. Chem.* **1981**, *13*, 329–348.
(10) Miller, I. R. In *Topics in Bioelectrochemistry and Bioenergetics*; Milazzo, G., Ed.; Wiley: Chichester, 1981; Vol. 4, pp 194–225.
(11) Nelson, A.; Benton, A. *J. Electroanal. Chem.* **1986**, *202*, 253–270.
(12) Moncelli, M. R.; Becucci, L.; Guidelli, R. *Biophys. J.* **1994**, *66*, 1969–1980.
(13) MacDonald, R. C.; Simons, S. A.; Baer, E. *Biochemistry* **1976**, *15*, 885–891.
(14) Ohki, S.; Kurland, R. *Biochim. Biophys. Acta* **1981**, *645*, 170–176.
(15) Matinyan, N. S.; Ershler, I. A.; Abido, I. G. *Biol. Membr.* **1985**, *1*, 451–477.
(16) Tsui, F. C.; Ojcius, D. M.; Hubbel, W. L. *Biophys. J.* **1986**, *49*, 459–468.
(17) Nelson, A.; Auffret, N. *J. Electroanal. Chem.* **1988**, *244*, 99–113.
(18) Nelson, A.; Auffret, N. *J. Electroanal. Chem.* **1988**, *248*, 167–180.
(19) Foresti, M. L.; Moncelli, M. R.; Guidelli, R. *J. Electroanal. Chem.* **1980**, *109*, 1–14.
(20) Carlà, M.; Sastre de Vicente, M.; Moncelli, M. R.; Foresti, M. L.; Guidelli, R. *J. Electroanal. Chem.* **1988**, *246*, 283–296.
(21) Liberman, E. A.; Topaly, V. P. *Biochim. Biophys. Acta* **1968**, *163*, 125–136.
(22) Neumcke, B.; Läuger, P. *Biophys. J.* **1969**, *9*, 1160–1170.
(23) Hauser, H.; Phillips, M. C. *Prog. Surf. Membr. Sci.* **1979**, *13*, 297–413.
(24) Grigor'ev, P. A.; Yermishkin, L. N.; Markin, V. S. *Exptl. Biofiz.* **1972**, *17*, 788–793.
(25) Wulf, J.; Benz, R.; Pohl, W. G. *Biochim. Biophys. Acta* **1977**, *465*, 429–442.
(26) Wang, C. C.; Bruner, L. J. *Biophys. J.* **1977**, *17*, 131–145.
(27) Barlow, C. A.; MacDonald, J. R. *Adv. Electrochem. Eng.* **1967**, *6*, 1–200.
(28) Tsien, R. Y.; Hladky, S. *Biophys. J.* **1982**, *39*, 49–56.
(29) Tsien, R. Y. *Biophys. J.* **1978**, *24*, 561–567.
(30) Wang, C. C.; Bruner, L. J. *Biophys. J.* **1978**, *24*, 749–764.
(31) Flewelling, R. F.; Hubbell, W. L. *Biophys. J.* **1986**, *49*, 541–552.
(32) Levine, S.; Mingings, J.; Bell, G. M. *J. Electroanal. Chem.* **1967**, *13*, 280–329.
(33) Levine, S.; Bell, G. M.; Calvert, D. *Can. J. Chem.* **1962**, *40*, 518–537.
(34) Levine, S.; Mingings, J.; Bell, G. M. *Can. J. Chem.* **1965**, *43*, 2834–2865.
(35) Levine, S.; Robinson, K.; Bell, G. M.; Mingins, J. *J. Electroanal. Chem.* **1972**, *38*, 253–269.
(36) Levine, S.; Robinson, K. *J. Electroanal. Chem.* **1973**, *41*, 159–177.

JP943313N